



# Covalent organic frameworks for modulating crystallization kinetics in perovskite photovoltaics

Xiao Liang<sup>a,b</sup>, Chaoqin Han<sup>b</sup>, Fei Wang<sup>a,b</sup>, Jiajun Wu<sup>a,b</sup>, Xianfang Zhou<sup>a,b</sup>, Haoran Lin<sup>b</sup>, Xiaoyuan Liu<sup>b,\*</sup>, Quanyao Zhu<sup>a,\*</sup>, Gang Li<sup>c,\*</sup>, Hanlin Hu<sup>b,\*</sup>

<sup>a</sup> State Key Laboratory of Advanced Technology for Materials Synthesis and Processing, School of Materials Science and Engineering, Wuhan University of Technology, Wuhan, China

<sup>b</sup> Hoffmann Institute of Advanced Materials, Shenzhen Polytechnic University, 7098 Liuxian Boulevard, Shenzhen 518055, China

<sup>c</sup> Department of Electronic and Information Engineering, Research Institute for Smart Energy (RISE), The Hong Kong Polytechnic University, Hung Hom, Kowloon, Hong Kong, China

## ARTICLE INFO

### Keywords:

Covalent organic frameworks  
In-situ UV-vis spectra  
High-quality perovskite films  
Perovskite Photovoltaics

## ABSTRACT

Covalent organic frameworks (COFs), recognized for their conjugated frameworks, adjustable porosity, and customizable functionalization, are emerging as versatile materials in perovskite photovoltaics with the potential to enhance both device performance and stability. However, a comprehensive understanding of their precise influence on the intricate phenomenon of perovskite crystallization kinetics is still lacking. In this study, we have successfully synthesized two distinctive COF materials, namely HIAM-0001 and HIAM-0004, utilizing the structural units of 5',5'''-(benzo[c] [1,2,5]thiadiazole-4,7-diyl)bis([1,1':3',1''-terphenyl]-4,4''-dicarbaldehyde)) (BT-TDA), with either the additional unit p-xylylenedicyanide (PDAN) or 2,2'-([2,2'-bipyridine]-5,5'-diyl) diacetonitrile (BPyDAN). By incorporating them into the PbI<sub>2</sub> layer, we have facilitated high-quality perovskite film fabrication through a two-step process. The COF-assisted PbI<sub>2</sub> films exhibited a distinct porous structure, facilitating organic salt solution permeation and reducing PbI<sub>2</sub> residues. Notably, *in-situ* UV-vis absorption characterization revealed slowed perovskite film crystallization kinetics with COF assistance, leading to the formation of larger crystal grains, fewer grain boundaries, reduced defect density, and suppressed non-radiative recombination, ultimately resulting in improved device performance. In comparison to HIAM-0001, the enhanced  $\pi$ - $\pi$  interactions of HIAM-0004, with its bipyridine-based unit, exhibited more pronounced interactions with the perovskite, contributing to a remarkable PCE of 24.06% and excellent device stability. This study underscores the pivotal role of COF modification in shaping perovskite film crystallization kinetics, thereby enhancing film quality, reducing defects, and boosting device stability.

## 1. Introduction

Perovskite solar cells (PSCs) have garnered significant attention within the scientific community due to their exceptional optoelectronic properties, cost-effectiveness, and straightforward processability [1–10]. The power conversion efficiency (PCE) of single-junction PSCs has experienced a rapid surge, reaching a certified value of 26.1 % [11]. One of the crucial factors behind the rapid PCE improvement lies in the optimization of film crystallization kinetics to mitigate crystallographic defects within the perovskite material [12–14]. Nonetheless, regulating the perovskite crystallization process remains a concern due to the unexpectedly high reaction rate constants observed among various

solution precursors [15,16].

The fast and uncontrolled formation of perovskite crystals introduces numerous crystallographic flaws, which can act as sites for non-radiative recombination, exerting detrimental effects on charge transfer, carrier longevity, and overall device performance [17,18]. Therefore, precise regulation of crystallization kinetics is crucial for achieving high-quality perovskite films with exceptional optoelectronic properties. A variety of additive strategies, including functional molecules [19,20], ionic liquids [21,22], and so on, are utilized to fine-tune the crystallization kinetics of PSCs [23–25]. Xu et al. [26] utilized Lewis base additives, which adjusted molecular interactions, leading to a delay in the perovskite crystallization process as observed through *in-situ* X-ray scattering. Chen

\* Corresponding authors.

E-mail addresses: [liuxiaoyuan1989@szpu.edu.cn](mailto:liuxiaoyuan1989@szpu.edu.cn) (X. Liu), [cglamri@whut.edu.cn](mailto:cglamri@whut.edu.cn) (Q. Zhu), [gang.w.li@polyu.edu.hk](mailto:gang.w.li@polyu.edu.hk) (G. Li), [hanlinhu@szpu.edu.cn](mailto:hanlinhu@szpu.edu.cn) (H. Hu).

<https://doi.org/10.1016/j.cej.2023.147235>

Received 1 September 2023; Received in revised form 1 November 2023; Accepted 7 November 2023

Available online 11 November 2023

1385-8947/© 2023 Elsevier B.V. All rights reserved.

et al. [27] incorporated a small amount of 1-methyl-2-pyrrolidinone to retard perovskite crystallization, resulting in enhanced crystallinity, vertical orientation, and a graded phase distribution. Qin and colleagues [28] precisely control the crystallization kinetics of perovskite film with sequential A-site doping of  $\text{Cs}^+$  and  $\text{GA}^+$ , promoting the phase transition and eliminating pinholes. However, these small additives present challenges in precisely controlling perovskite crystallization and simultaneously passivating defects.

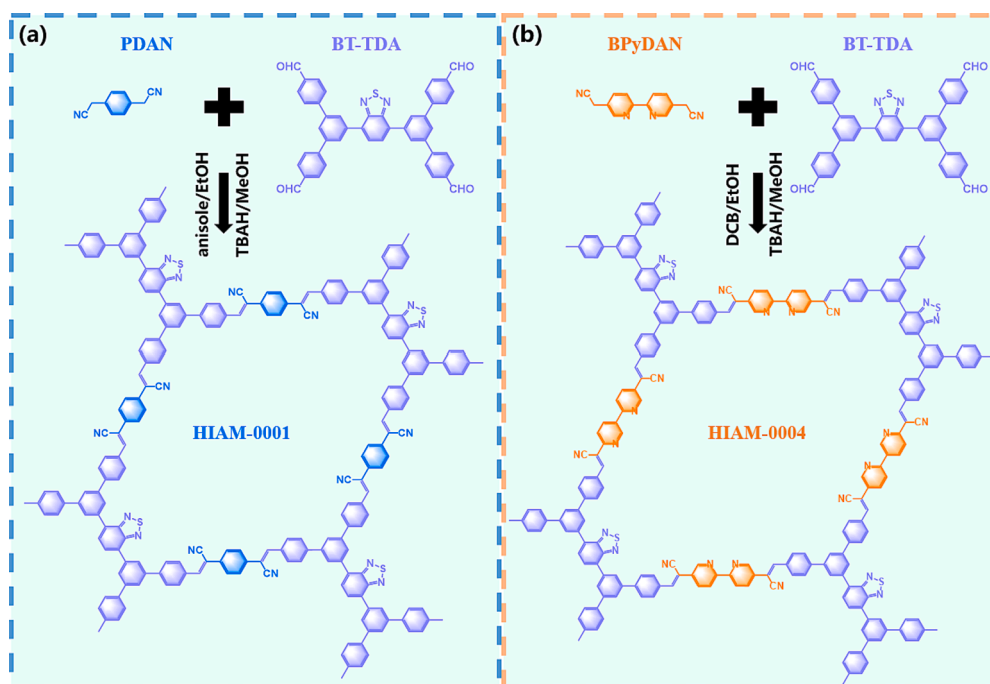
Covalent organic frameworks (COFs) represent a growing class of crystalline porous polymers, characterized by intricate  $\pi$ -conjugated systems, periodic frameworks, and distinct pores [29,30]. These COF materials not only act as regulators for controlling the perovskite crystallization kinetics but also enhance the stability of perovskite materials [31–33], owing to their distinctive porous framework structure. He et al. [34] were the first to *in-situ* synthesize a 2D COF within the  $\text{PbI}_2$  layer, enabling precise regulation of the crystallization process of perovskite film, reducing defect density, and promoting carrier transport. Nie et al. [35] synthesized and introduced TTDA-TTA-COF into the perovskite layer to improve charge separation by creating spatially separate frontier orbitals and effectively inhibiting degradation of the  $\text{FAPbI}_3$  layer, preventing the formation of  $\delta$ - $\text{FAPbI}_3$  and enhancing long-term stability. Gou and colleagues [36] introduced an innovative dual-interface modulation approach, harnessing sulfhydryl functionalization within HS-COFs to prepare high-quality perovskite films with reduced surface defects, thereby augment the efficiency and stability of PSCs. While the incorporation of COFs has demonstrated promise in improving the stability and optoelectronic characteristics of PSCs, there is a lack of in-depth knowledge of their precise influence on the complex phenomenon of perovskite crystallization kinetics.

Herein, two unique COF materials were designed and synthesized, as shown in Scheme 1. The synthesis of HIAM-0001 and HIAM-0004 involved the utilization of p-xylylenedicyanide (PDAN), 2,2'-(1,2'-bipyridine)-5,5'-diyl diacetonitrile (BPyDAN), and 5',5'''-(benzo [c][1,2,5]thiadiazole-4,7-diyl) bis (([1,1':3',1''-terphenyl]-4,4''-dicarbaldehyde)) (BT-TDA). These COFs integrated into the  $\text{PbI}_2$  layer to facilitate a distinctive porous architecture, which notably facilitated the permeation of the organic salt solution during the second step and reduced the amount of  $\text{PbI}_2$  residues. Intriguingly, we observed a delay in

crystallization kinetics that remarkably favored the formation of high-quality perovskite films characterized by larger crystal grains and fewer grain boundaries *via in-situ* UV-vis characterization. Moreover, compared to the HIAM-0001 sample, HIAM-0004, with its bipyridine-based unit, exhibits enhanced conjugation and stronger  $\pi$ - $\pi$  interactions, leading to more pronounced interactions with the perovskite with a remarkable PCE of 24.06 %, along with exceptional stability. This study emphasizes the crucial role of COF assistance in expertly fine-tuning perovskite film crystallization kinetics, ultimately achieving high-quality film and enhanced device photovoltaic performance.

## 2. Results and discussion

As shown in Fig. 1(a,b), the crystallinity of HIAM-0001 and HIAM-0004 was explored through powder X-ray diffraction (PXRD) measurements. The main characteristic diffraction peak positions of HIAM-0001 and HIAM-0004 are at  $3.42^\circ$  and  $2.96^\circ$ , respectively, both corresponding to the (1 1 0) crystal planes, demonstrating excellent crystalline performance consistent with our previous literature reports [37,38]. The experimental PXRD patterns of HIAM-0001 and HIAM-0004 matched well with the simulated patterns from the AA-staggered stacking model (black), which provided good agreement factors (HIAM-0001, Rwp = 5.58 % and Rp = 3.66 %; HIAM-0004, Rwp = 4.52 %, and Rp = 2.66 %) with the optimized parameters (HIAM-0001, a = 27.02 Å, b = 27.01 Å, c = 7.17 Å,  $\alpha = 89.96^\circ$ ,  $\beta = 90.01^\circ$ , and  $\gamma = 90.02^\circ$ ; HIAM-0004, a = 31.51 Å, b = 31.52 Å, c = 7.12 Å,  $\alpha = 85.85^\circ$ ,  $\beta = 87.48^\circ$ , and  $\gamma = 90.11^\circ$ ). It is noteworthy that the scanning electron micrographs (SEM) demonstrate a comparable needle-like structure for both COF materials (Fig. 1c, d). The structural characterization of the resulting COF material was carried out through Fourier transform infrared (FTIR) spectroscopy (Fig. S1). We can observe from the FTIR spectra that both COFs formed by HIAM-0001 and HIAM-0004 exhibit new distinctive peaks at positions  $2220\text{ cm}^{-1}$  and  $2210\text{ cm}^{-1}$ , respectively. These characteristic peaks are indicative of the  $\text{C}\equiv\text{N}$  stretching vibration in the vinyl cyano group, providing clear evidence of successfully synthesizing  $\text{SP}^2$  carbon-conjugated COFs [37]. Additionally, the Brunauer–Emmett–Teller (BET) surface areas of HIAM-001 and HIAM-004 were calculated to be 511 and  $397\text{ m}^2/\text{g}$ , respectively (Fig. 1 e, f), and the pore size distributions were



Scheme 1. COF molecular structure design of (a) HIAM-0001 and (b) HIAM-0004.

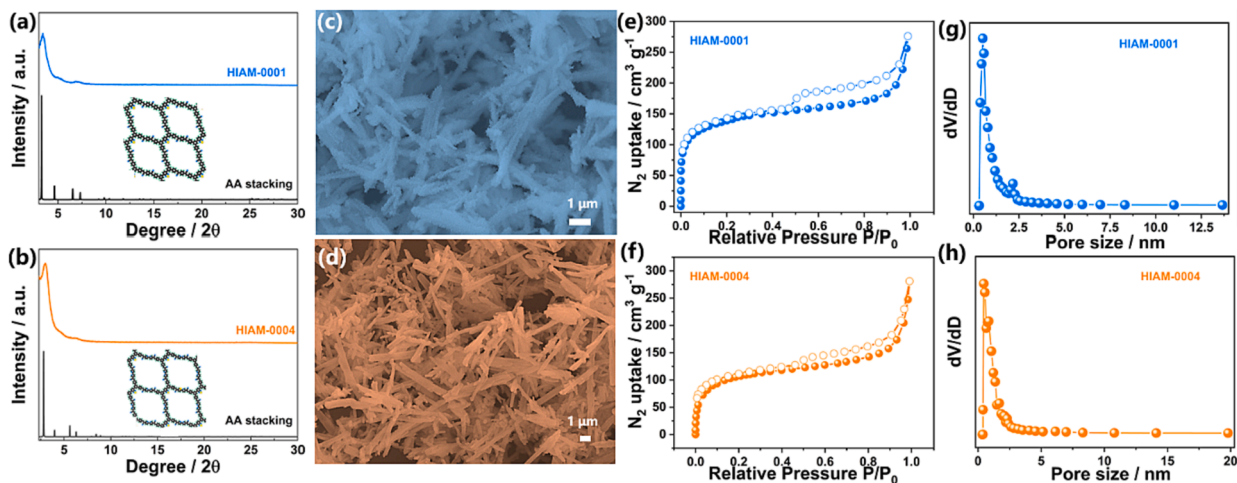


**Fig. 1.** Powder X-ray diffraction (PXRD) patterns of experimentally observed (blue or orange) and AA stacking mode (black) (a) HIAM-0001 and (b) HIAM-0004. Scanning electron micrographs (SEM) images of the (c) HIAM-0001 and (d) HIAM-0004. Nitrogen adsorption–desorption isotherms and pore size distribution profiles of (e,g) HIAM-0001 and (f,h) HIAM-0004. (For interpretation of the references to colour in this figure legend, the reader is referred to the web version of this article.)

obtained stemming from the nonlocal density functional theory (NLDFT) model from the nitrogen isotherm at about 0.51 and 0.45 nm (Fig. 1 g, h). The steady-state photoluminescence (PL) and absorption spectra,

both types of COFs exhibit a congruent maximum PL excitation peak at 565 nm, along with an absorption range spanning 300 nm to 500 nm (Fig. S2). This parallelism in their PL and absorption characteristics

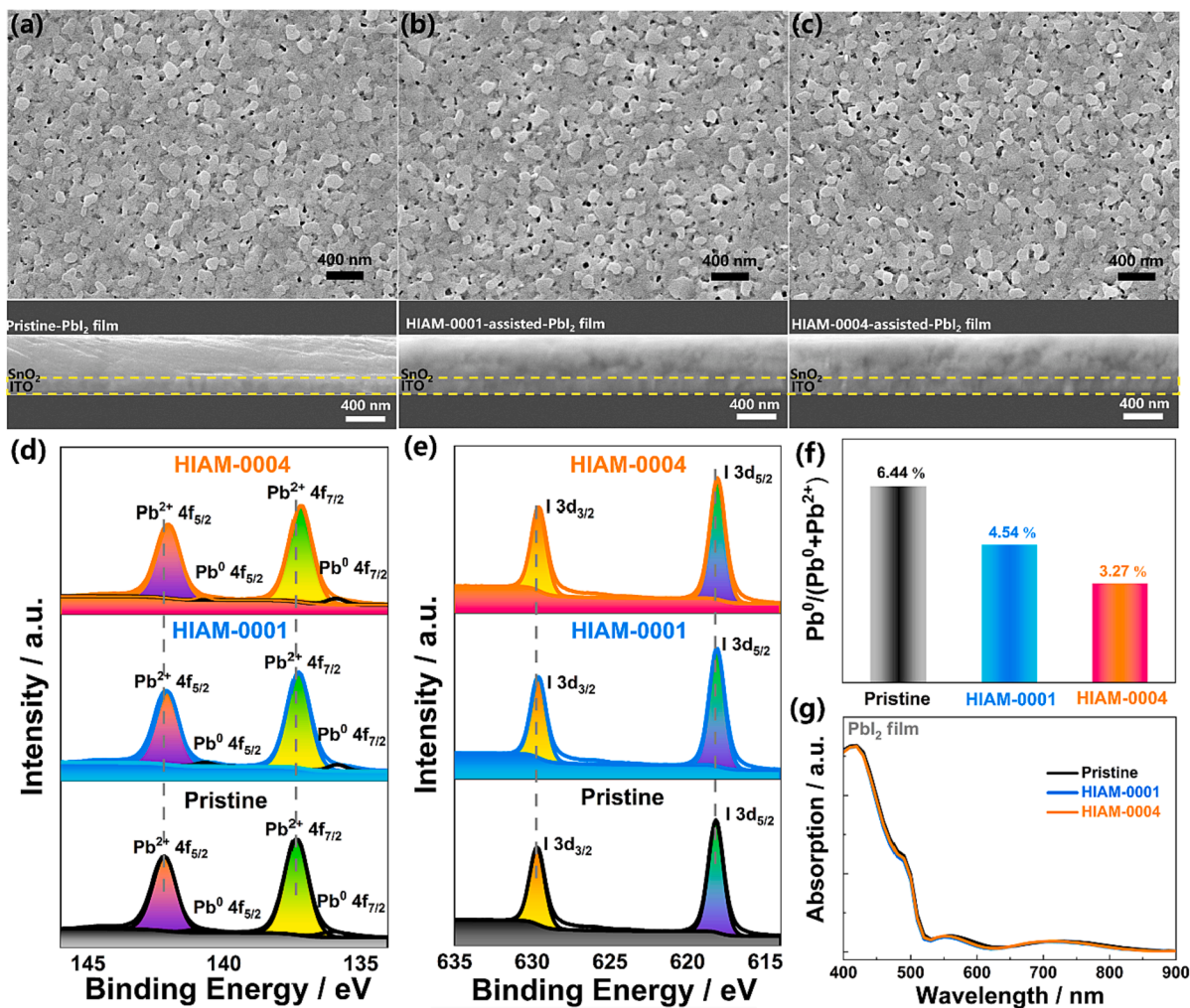


**Fig. 2.** Surface (up) and cross-section (down) SEM images of the (a) pristine, (b) HIAM-0001, and (c) HIAM-0004-assisted PbI<sub>2</sub> film. X-ray photoelectron spectroscopy (XPS) measurements of (d) Pb 4f and (e) I 3d. (f) The fitted results of the Pb<sup>0</sup>/(Pb<sup>0</sup> + Pb<sup>2+</sup>) ratio, and (g) UV-vis absorption spectra of PbI<sub>2</sub> film.



highlights the shared optical properties between the two COFs, signifying a consistent response to excitation and light absorption within this spectral range. This alignment further emphasizes the potential for similar optoelectronic behavior and applications in both materials. The decomposition temperatures ( $T_d$ , 5 % mass loss), as indicated in Fig. S3, are 351.8 °C for HIAM-0001 and 382.1 °C for HIAM-0004 powder. These values signify the elevated thermostability of both materials. Interestingly, HIAM-0004 exhibits a higher decomposition temperature, pointing to its enhanced resistance to thermal volatilization compared to HIAM-0001.

To visualize the influence of HIAM-0001 and HIAM-0004 materials on the morphology of  $\text{PbI}_2$  films, both top-view SEM and cross-sectional SEM tests were conducted. The pristine  $\text{PbI}_2$  layer exhibited a naturally compact and dense structure (Fig. 2a). In contrast, the  $\text{PbI}_2$  films deposited on HIAM-0001 and HIAM-0004 displayed additional nanometer-scale micropores, thereby providing enhanced pathways for the percolation of the organic precursor solution (Fig. 2b,c). These observations align with our earlier findings [39]. Furthermore, X-ray photoelectron spectroscopy (XPS) characterization was utilized to further elucidating the chemical impact of the COF on the perovskite surface. The entire spectra and S 2p spectra are presented in Fig. S4, while the surface Pb 4f core level of the corresponding pristine samples is depicted in Fig. 2(d). The dominant peaks (137.3 eV for  $4f_{7/2}$  and 142.1 eV for  $4f_{5/2}$ ) correspond to  $\text{Pb}^{2+}$  components with saturated

coordination, and the minor peaks at a lower binding energy (135.8 eV for  $4f_{7/2}$  and 140.7 eV for  $4f_{5/2}$ ) are indicative of metallic Pb clusters ( $\text{Pb}^0$ ) [40]. In comparison to the pristine sample, HIAM-0001 and HIAM-0004-assisted  $\text{PbI}_2$  films exhibited lower energy level shifts of approximately 0.1 eV, and 0.2 eV, respectively. Our findings suggest that the HIAM-0004-assisted  $\text{PbI}_2$  films demonstrates the highest shift of the Pb 4f peak towards lower binding energy, indicative of a stronger interaction. Simultaneously, the I 3d peaks of the perovskite material exhibit a comparable shift upon the integration of COFs (Fig. 2e). This shift implies a reduction in the electron-withdrawing capability of the Pb atoms, underscoring the impact of COF incorporation on the electronic properties of the perovskite structure [36,41]. The presence of the HIAM-0001 and HIAM-0004 in the target film was confirmed by characteristic peaks for  $\text{S}^{2-}$  at approximately 165.3 eV (Fig. S4b) [42]. We further assessed the  $\text{Pb}^0/(\text{Pb}^0 + \text{Pb}^{2+})$  ratio for the pristine (6.44 %), HIAM-0001-assisted (4.54 %), and HIAM-0004-assisted (3.27 %) samples based on the integrated peak areas from the XPS spectra (Fig. 2f). This result suggests effective suppression of metallic  $\text{Pb}^0$  via COF-assisted methods, with HIAM-0004-assisted suppression being the most efficient. The UV-vis absorption spectra for both pristine and COF-assisted  $\text{PbI}_2$  and perovskite thin films showed no noticeable differences (Fig. 2g). To assess the crystal structures and orientations of the pristine and COF-assisted  $\text{PbI}_2$  thin films, XRD and GIWAXS analyses were conducted (Fig. S5). In both cases, the  $\text{PbI}_2$  films exhibited a distinct

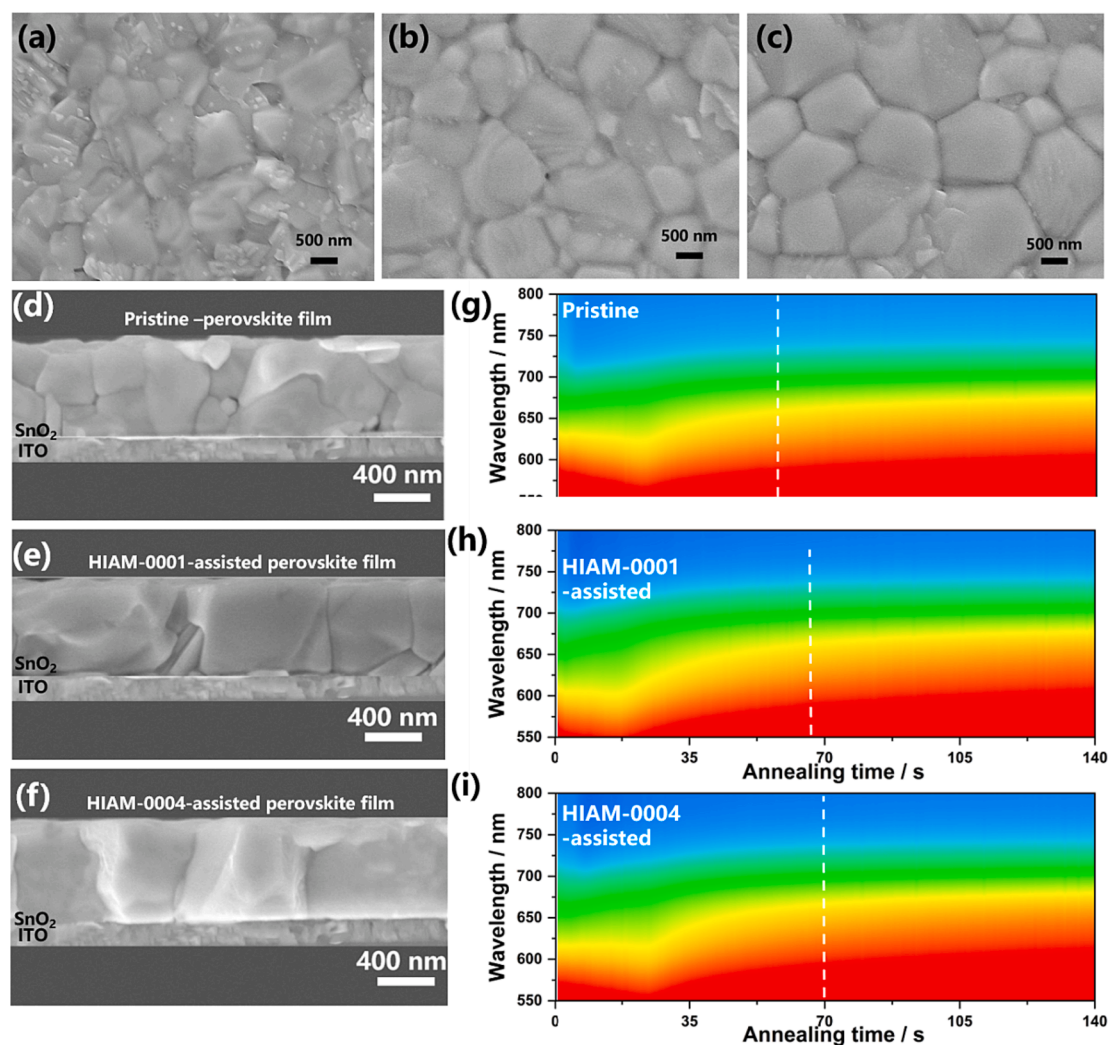


**Fig. 3.** Surface (a-c), cross-section (d-f) SEM images, and *In-situ* UV-vis absorption spectra acquired during the annealing process of the (a,d,g) pristine, (b,e,h) HIAM-0001, and (c,f,i) HIAM-0004-assisted perovskite film.

diffraction peak at  $12.8^\circ$  along with a scattering peak at  $q = 0.9 \text{ \AA}^{-1}$ . This scattering peak corresponds to the (001) lattice plane of crystallized  $\text{PbI}_2$ . This outcome demonstrates that the addition of COF did not alter the crystal structure or orientation of  $\text{PbI}_2$  crystals.

The surface and cross-section SEM morphology of the perovskite films on  $\text{SnO}_2$  surfaces is depicted in Fig. 3(a–f). For the pristine sample, distinctive bright white  $\text{PbI}_2$  crystals and small grains (approximately 300–400 nm) are clearly visible. Compared to the benzene rings in PDAN, the bipyridine units in BPyDAN exhibit stronger chemical reactivity, potentially leading to enhanced conjugation and more pronounced  $\pi$ - $\pi$  interactions in HIAM-0004. As a result, HIAM-0004 might facilitate the perovskite to achieve a higher degree of crystallinity. In the case of the HIAM-0004-assisted perovskite films, larger grain sizes (around 600–700 nm) and no presence of  $\text{PbI}_2$  on the perovskite surface are detected. The corresponding cross-sectional SEM images (Fig. 3d–f) of the HIAM-0001 and HIAM-0004-assisted perovskite films display conspicuous large grains and fewer grain boundaries compared to the pristine samples, aligning with the observations from the top-view images. To gain further insights into the effective enhancement of perovskite grain size through the introduction of COF, we employed *in-situ* UV–vis characterization to dynamically monitor the crystallization kinetics of the pristine, HIAM-0001, and HIAM-0004-assisted perovskite films as illustrated in Fig. 3g–i. The spectral intensity within the 550 to 800 nm range gradually increased throughout the annealing process, indicating the formation of the black perovskite phase. For the pristine film, the perovskite conversion was fully completed in 53 s, accompanied by a simultaneous broadening and enhancement of the absorption spectrum. In contrast, the conversion within the HIAM-0001 and HIAM-0004-assisted perovskite films was delayed, taking 68 and 70 s, respectively, indicating the presence of an intermediate adduct that appeared to impede the crystallization process. This may be due to interactions between the S, N elements within COF material and Pb, I elements within perovskite. During the early stages of crystal growth in the solution,  $\text{S}^{2-}$  coordinates with  $\text{Pb}^{2+}$ , and  $\text{N}^+$  coordinates with  $\text{I}^-$ . Subsequently, during the annealing process,  $\text{S}^{2-}$ - $\text{Pb}^{2+}$  and  $\text{N}^+$ - $\text{I}^-$  gradually get replaced by  $\text{Pb}^{2+}$ - $\text{I}^-$ , thus decelerating the crystallization kinetics of the perovskite film. Eventually,  $\text{S}^{2-}$ - $\text{Pb}^{2+}$  and  $\text{N}^+$ - $\text{I}^-$  are entirely

substituted by  $\text{Pb}^{2+}$ - $\text{I}^-$ , completing the crystal growth. These comprehensive findings collectively emphasize the effectiveness of the HIAM-0001 and HIAM-0004 strategies in slowing down the crystallization rate of perovskite films, ultimately leading to a noticeable improvement in film quality. The UV–vis absorption spectra of the films after thermal annealing are provided in the Fig. S6a. The bandgap, as determined from the Tauc plots (Fig. S6b), remain consistent at 1.57 eV, 1.57 eV, and 1.56 eV for the pristine, HIAM-0001, and HIAM-0004-assisted perovskite films, respectively. This suggests that the introduction of a small quantity of COF does not induce notable changes in the bandgap of the perovskite.

Subsequent to this, the analysis using GIWAXS brings out a noticeable distinction in the scattering peaks exhibited by the three examined samples. Unlike the pristine sample, depicted in Fig. 4a, the perovskite films assisted by HIAM-0001 and HIAM-0004 show a significant reduction in the intensity of the scattering ring at a low  $q$  value of  $0.9 \text{ \AA}^{-1}$ , as seen in Fig. 4b and 4c. This particular  $q$  value corresponds to the (001) lattice plane of  $\text{PbI}_2$  crystals. This observation stands as direct confirmation that the incorporation of HIAM-0001 and HIAM-0004 aids in the transformation of  $\text{PbI}_2$  into perovskite material, ultimately leading to an almost negligible presence of residual  $\text{PbI}_2$  in the final perovskite film. For better visualization, radial integration curves were generated based on the corresponding GIWAXS patterns, as shown in Fig. 4d. Notably, a robust scattering peak at  $q = 1.0 \text{ \AA}^{-1}$  is apparent in both samples, attributed to the (110) plane of perovskite crystals. However, in the case of the original sample, there is a distinct scattering peak at  $q = 0.9 \text{ \AA}^{-1}$  alongside the (110) scattering peak, indicating the coexistence of (001)  $\text{PbI}_2$  crystals, as mentioned earlier. In contrast, the samples assisted by HIAM-0001 and HIAM-0004 exhibit a weak scattering peak at the same  $q = 0.9 \text{ \AA}^{-1}$  position, indicating minimal presence of  $\text{PbI}_2$  residuals in the final perovskite film. The enhanced conversion of  $\text{PbI}_2$  into perovskite material with the assistance of HIAM-0001 and HIAM-0004 can be attributed to the altered morphology of  $\text{PbI}_2$ , which is characterized by distributed pinholes, as discussed earlier. This modified morphology facilitates the effective penetration of the organic salt solution into the underlying  $\text{PbI}_2$  during the second-step deposition, leading to an improved contact between  $\text{PbI}_2$  and the

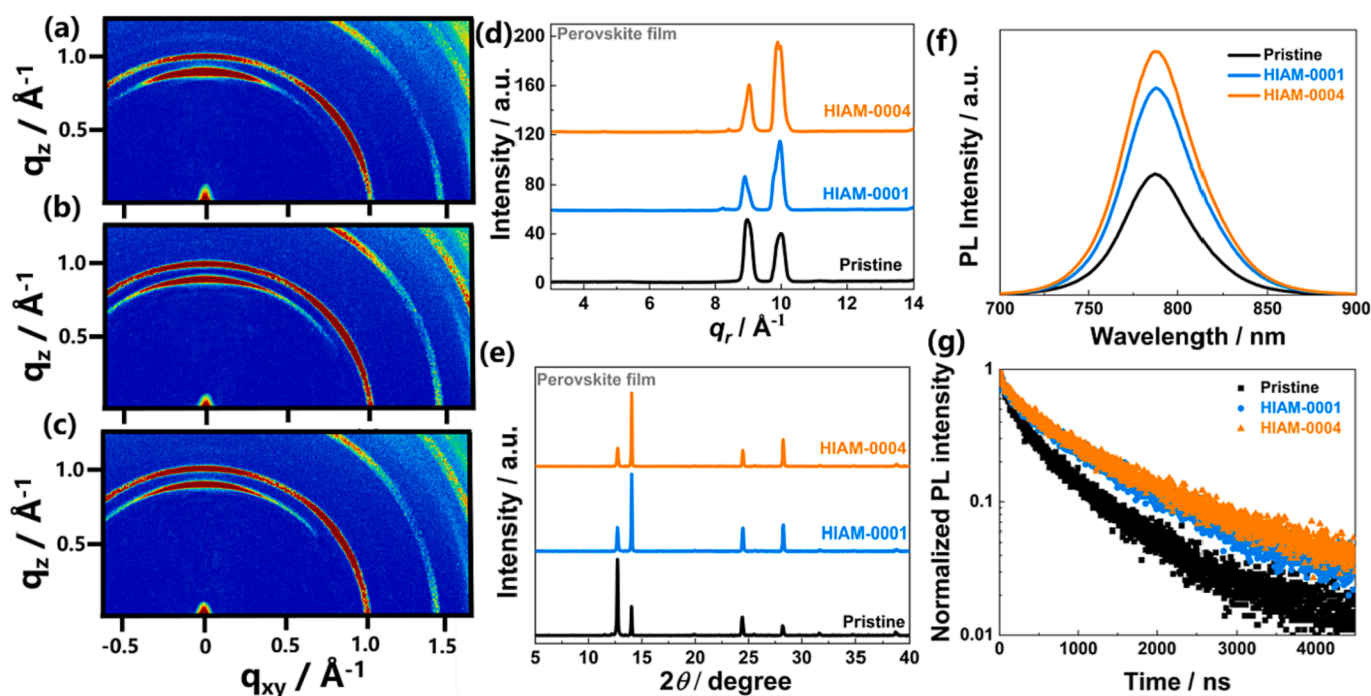
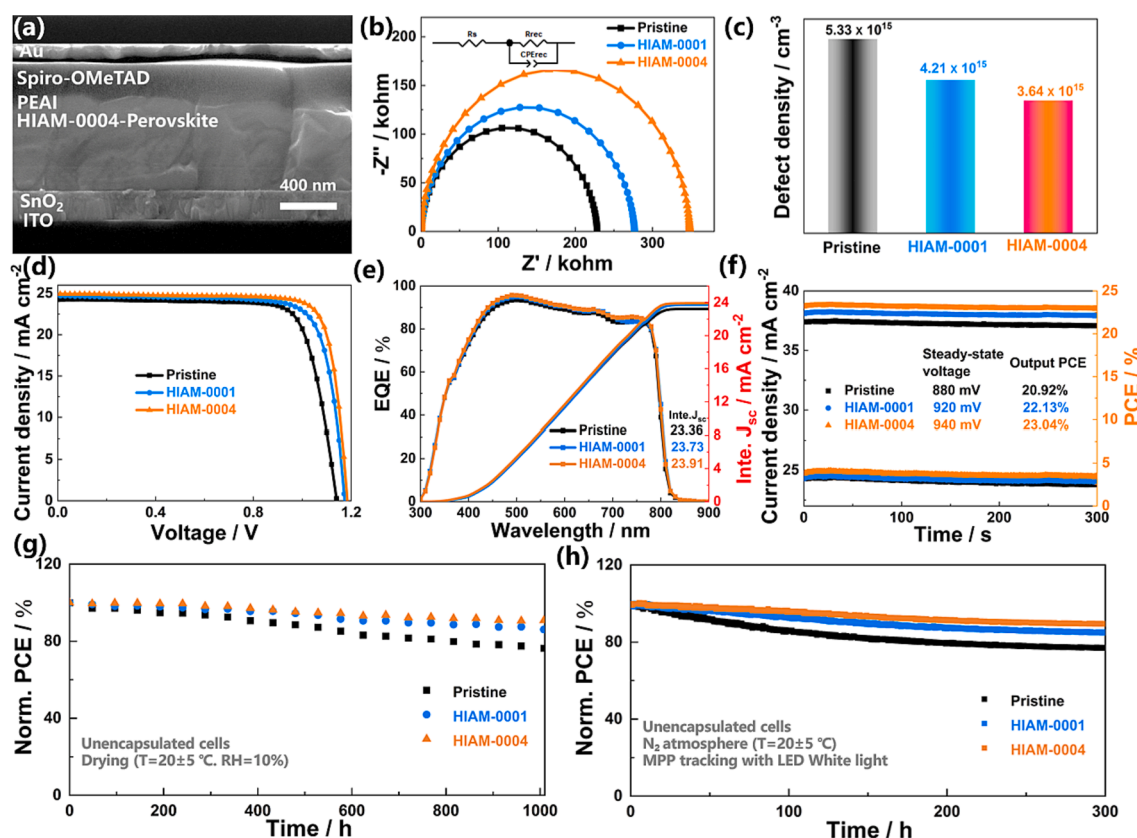


Fig. 4. The GIWAXS graphics of (a) pristine, (b) HIAM-0001, and (c) HIAM-0004-assisted perovskite film. (d) Radial integration and (e) XRD of both pristine, HIAM-0001, and HIAM-0004-assisted perovskite film from GIWAXS patterns. (f) Steady-state photoluminescence (PL) spectra. (g) Time-resolved PL decay curves.

organic salt. Consequently, the conversion of  $\text{PbI}_2$  into perovskite material is expedited. The XRD findings are in alignment with the GIWAXS results discussed earlier (Fig. 4e). Additionally, we conducted steady-state photoluminescence (PL) and time-resolved PL (TRPL) measurements to explore the carrier dynamic process and charge recombination behavior. Compared with the pristine and HIAM-0001-assisted perovskite film, HIAM-0004-assisted samples demonstrate significantly enhanced PL intensity (Fig. 4e) and a longer TRPL charge carrier lifetime (Fig. 4f), attributed to the passivation of trap states and the suppression of nonradiative recombination. The TRPL spectrum was fitted to the experimental data using a bi-exponential function (Fig. S7), and the fitting parameters are summarized in Table S1 of the Supporting Information.

To evaluate a correlation between the incorporation of COF in perovskite films and device performance, we integrated the aforementioned absorber layers into an entirely photovoltaic device featuring the standard configuration of  $\text{ITO}/\text{SnO}_2/\text{HIAM-0004-assisted perovskite}/\text{PEAI}/\text{Spiro-OMeTAD}/\text{Au}$ , as supported by the cross-sectional SEM micrographs depicted in Fig. 5a. The cross-sectional structures of the pristine devices exhibit similarity, with the only prominent distinction being the considerably enlarged grain size observed in the perovskite layer for the HIAM-0004-assisted configuration (Fig. S8). To assess the interfacial properties of PSC, electrochemical impedance spectroscopy (EIS) is performed under dark conditions without bias, employing a corresponding equivalent circuit model (Fig. 5b). The HIAM-0004-assisted device reveals an improvement in  $R_{\text{rec}}$  compared to the pristine and HIAM-0001 devices, indicating enhanced charge transport and suppressed charge recombination at the contact interface. To quantify

the extent of trap states, we utilized the space-charge-limited current (SCLC) model in hole-only device configurations (Fig. S9). The resulting trap density ( $N_t$ ) is assessed to be  $5.33$ ,  $4.21$  and  $3.64 \times 10^{15} \text{ cm}^{-3}$ , indicating that HIAM-0004 effectively reduces the interface defect density (Fig. 5c). The overview of the photovoltaic parameters for different concentrations of HIAM-0004 are illustrated in Table S2. As depicted in Fig. 5d, the optimized pristine exhibits a PCE of 21.61 % with an open-circuit voltage ( $V_{\text{oc}}$ ) of 1.147 V, a short-circuit current density ( $J_{\text{sc}}$ ) of  $24.22 \text{ mA cm}^{-2}$ , and a fill factor (FF) of 77.81 %. In contrast, the HIAM-0004-assisted device achieves a decent PCE of 24.06 % with a  $V_{\text{oc}}$  of 1.182 V, a  $J_{\text{sc}}$  of  $24.92 \text{ mA cm}^{-2}$ , and an FF of 81.69 % (Table S3). Additionally, we provide the recently reported COFs/MOFs-assisted PSCs with details listed in Table S4. The external quantum efficiency (EQE) spectra of the devices were recorded (Fig. 5e). The integrated current densities for the pristine, HIAM-0001 and HIAM-0004-assisted cells were measured to be 23.36, 23.73 and  $23.91 \text{ mA cm}^{-2}$ , respectively. In order to obtain a more detailed information in EQE spectra, we magnified the EQE spectra within the wavelength range of 400–800 nm (Fig. S10). This magnification distinctly reveals the enhanced EQE values in COF-assisted perovskite devices within the 400–700 nm wavelength range, attributing to the presence of robust conjugated structures and strong  $\pi$ - $\pi$  interactions [43]. The increase in the 700–800 nm wavelength range is a result of the improved quality of the perovskite film [44]. Owing to the eduction in defect states and effective suppression of non-radiative recombination, there is a noticeable enhancement in both the  $J_{\text{sc}}$  of the COF-assisted perovskite devices [45–47]. The statistical distributions of photovoltaic parameters of pristine and HIAM-0004-assisted devices are shown in Fig. S11. The



**Fig. 5.** (a) The cross-sectional SEM micrographs depict the layered structure of the fabricated devices, consisting of  $\text{ITO}/\text{SnO}_2/\text{HIAM-0004-assisted perovskite}/\text{PEAI}/\text{Spiro-OMeTAD}/\text{Au}$ . (b) The Nyquist plot derived from electrochemical impedance spectroscopy (EIS) provides a visual representation of the distinctions seen among pristine, HIAM-0001, and HIAM-0004-assisted PSCs. (c) Trap density ( $N_t$ ). (d) The current density–voltage ( $J$ – $V$ ) curves under AM1.5G solar simulator conditions, and (e) corresponding EQE spectra. (f) The stabilized power outputs for pristine, HIAM-0001 and HIAM-0004-assisted devices were measured at 0.88 V, 0.92 V and 0.94 V, respectively. (g) The normalized PCE of unencapsulated cells in dry circumstances (10 % relative humidity). (h) Non-encapsulated devices subjected to continuous illumination (1 sun) close to the maximum power point of a white LED lamp at  $20 \pm 5^\circ\text{C}$  in a nitrogen atmosphere.



HIAM-0004-assisted ( $PCE_{ave.} = 23.82\%$ ) devices deliver better repeatability with a tighter distribution and higher average PCE than the pristine ( $PCE_{ave.} = 21.03\%$ ) and HIAM-0001-assisted ( $PCE_{ave.} = 22.53\%$ ) devices. Furthermore, we selected the top 5 devices from each of the three types (20 solar cells of each type), for stability testing and error bar analysis (Fig. S12). Over a 120-hour period in a dry air environment, the COF-assisted perovskite devices displayed outstanding stability and smaller error bars compared to the pristine samples with larger error bars. This indicates a high level of repeatability for the COF-assisted perovskite devices. The devices were operated at their maximum power point (MPP) with applied biases of 0.88 V, 0.92 V and 0.94 V to monitor the stabilized power output. In the pristine and HIAM-0001 samples, a stable PCE of 20.92 % and 22.13 %, respectively, was observed, while the HIAM-0004-assisted device demonstrated an enhanced PCE of 23.04 % during the 300-second stabilization period (Fig. 5f). Subsequently, the operational stability of both the pristine, HIAM-0001 and HIAM-0004-assisted unencapsulated devices was assessed in a dark and dry environment and full sunlight soaking under continuous MPP tracking. After 1000 h of continuous operation in a dark and dry environment ( $20 \pm 2\text{ }^{\circ}\text{C}$ , 10 % RH), the HIAM-0004-assisted device exhibited remarkable capability to maintain 90.81 % of its initial PCE. In contrast, the pristine and HIAM-0001-assisted devices exhibit a much lower retention rate, with only 76.35 % and 86.12 %, respectively (Fig. 5g). Furthermore, the unencapsulated devices were also measured by tracking the true MPP tracking under continuous one-sun illumination with 1-Sun intensity at  $20 \pm 5\text{ }^{\circ}\text{C}$  in an  $N_2$  atmosphere. The HIAM-0004-assisted device maintained 89.4 % of its initial PCE after 300 h, whereas that of the pristine and HIAM-0001-assisted cell decreased to 22.8 % and 15.9 % of their original value, as depicted in Fig. 5h.

### 3. Conclusion

In summary, two COF materials, HIAM-0001 and HIAM-0004, were synthesized from BT-TDA structural units and incorporated into the  $PbI_2$  layer, which improved perovskite film quality through a two-step fabrication process. The COF-assisted  $PbI_2$  films exhibited a unique porous structure that enhanced permeation of organic salt and reduced  $PbI_2$  residues. Importantly, the COF assistance slowed perovskite crystallization, leading to the formation of larger perovskite grains with fewer boundaries, reduced defects, and the suppression of non-radiative recombination. The stronger  $\pi$ - $\pi$  interactions in HIAM-0004 led to a remarkable PCE of 24.06 % and enhanced device stability. This study underscores the crucial role of COF modification in perovskite film crystallization kinetics, resulting in improved film quality with increased device stability.

### Declaration of Competing Interest

The authors declare that they have no known competing financial interests or personal relationships that could have appeared to influence the work reported in this paper.

### Data availability

The authors do not have permission to share data.

### Acknowledgments

This work is supported by the Scientific Research Startup Fund for Shenzhen High-Caliber Personnel of Shenzhen Polytechnic, No. 6022310038k and 6022310049k. The financial support from the National Natural Science Foundation of China (No. 62004129), Guangdong Basic and Applied Basic Research Foundation (No. 2023A1515011677), Shenzhen Science and Technology Innovation Commission (Project No. JCYJ20200109105003940 ; Project No. 20220811205532001),

Research Grants Council of Hong Kong (GRF grant 15221320, CRF C5037-18G, C7018-20G); the Hong Kong Polytechnic University funds (Sir Sze-yuen Chung Endowed Professorship Fund (8-8480), and RISE (Q-CDA5)) is gratefully acknowledged.

### Appendix A. Supplementary data

Supplementary data to this article can be found online at <https://doi.org/10.1016/j.cej.2023.147235>.

### References

- [1] Z. Yang, X. Cao, G. Niu, Y. Wang, Y. Dong, S. Cao, W. Liu, X. Wang, Y. Liu, J. Wang, Removing residual  $PbI_2$  on the perovskite surface for efficient solar cells, *Chem. Eng. J.* 464 (2023), 142720, <https://doi.org/10.1016/j.cej.2023.142720>.
- [2] H. Guo, X. Yang, J. Zhu, Z. An, O.Y. Gong, Z. Li, P.J. Yoo, S. Kim, G.S. Han, H. S. Jung, Bifunctional modified biopolymer for highly efficient and stable perovskite solar cells and modules, *Chem. Eng. J.* 460 (2023), 141699, <https://doi.org/10.1016/j.cej.2023.141699>.
- [3] R. Zhuang, L. Wang, J. Qiu, L. Xie, X. Miao, X. Zhang, Y. Hua, Effect of molecular configuration of additives on perovskite crystallization and hot carriers behavior in perovskite solar cells, *Chem. Eng. J.* 463 (2023), 142449, <https://doi.org/10.1016/j.cej.2023.142449>.
- [4] L. Li, R. Zhang, Z. Wu, Y. Wang, J. Hong, H. Rao, Z. Pan, X. Zhong, Crystallization control of air-processed wide-bandgap perovskite for carbon-based perovskite solar cells with 17.69% efficiency, *Chem. Eng. J.* 455 (2023), 140566, <https://doi.org/10.1016/j.cej.2022.140566>.
- [5] D.W. Kim, Y.W. Noh, J. Han, H.S. Kim, C.H. Jang, J.A. Hong, S. Park, M.H. Lee, Y. I. Kim, M.H. Song, Efficient MAPbI<sub>3</sub>-based perovskite solar cells exceeding 21% efficiency via aging treatment, *Chem. Eng. J.* 475 (2023), 146451, <https://doi.org/10.1016/j.cej.2023.146451>.
- [6] F. Wang, P. Wai-Keung Fong, Z. Ren, H.-L. Xia, K. Zhou, K. Wang, J. Zhu, X. Huang, X.-Y. Liu, H. Wang, Y. Shi, H. Lin, Q. Zhu, G. Li, H. Hu, In-depth understanding of ionic liquid assisted perovskite film formation mechanism for two-step perovskite photovoltaics, *J. Energy Chem.* 73 (2022) 599–606, <https://doi.org/10.1016/j.jechem.2022.06.040>.
- [7] F. Wang, C. Ge, D. Duan, H. Lin, L. Li, P. Naumov, H. Hu, Recent progress in ionic liquids for stability engineering of perovskite solar cells, *Small Struct.* 3 (2022) 2200048, <https://doi.org/10.1002/ssstr.202200048>.
- [8] Y. Zhu, G. Chen, Y. Chu, C. Hsu, J. Wang, C. Tung, H.M. Chen, Hetero-atomic pairs with a distal  $Fe^{3+}$ -site boost water oxidation, *Angew. Chemie.* 134 (2022), <https://doi.org/10.1002/ange.202211142>.
- [9] Y. Zhu, K. Fan, C. Hsu, G. Chen, C. Chen, T. Liu, Z. Lin, S. She, L. Li, H. Zhou, Y. Zhu, H.M. Chen, H. Huang, Supported ruthenium single-atom and clustered catalysts outperform benchmark Pt for alkaline hydrogen evolution, *Adv. Mater.* 35 (2023), <https://doi.org/10.1002/adma.202301133>.
- [10] Y. Zhu, T.-R. Kuo, Y.-H. Li, M.-Y. Qi, G. Chen, J. Wang, Y.-J. Xu, H.M. Chen, Emerging dynamic structure of electrocatalysts unveiled by in situ X-ray diffraction/absorption spectroscopy, *Energy Environ. Sci.* 14 (2021) 1928–1958, <https://doi.org/10.1039/D0EE03903A>.
- [11] NREL. Best research-cell efficiency chart, NREL. Best research-cell efficiency chart, (2023) [www.nrel.gov/best-research-cell-efficiencies](https://www.nrel.gov/best-research-cell-efficiencies). <https://doi.org/https://www.nrel.gov/pv/assets/pdfs/best-research-cell-efficiencies>.
- [12] H. Wang, Z. Wang, X. Tang, L. Liu, H. Zhang, X. Yao, F. Wang, S. Wu, X. Liu, Understanding the doping effect in  $CsPbI_2Br$  solar cells: crystallization kinetics, defect passivation and energy level alignment, *Chem. Eng. J.* 453 (2023), 139952, <https://doi.org/10.1016/j.cej.2022.139952>.
- [13] J. Deng, H. Zhang, L. Yang, K. Wei, X. Zhang, Y. Yang, J. Zhang, Additive strategy to regulate crystallization and charge carrier dynamics of  $CsBi_{3}I_{10}$  towards efficient and stable thin film solar cells, *Chem. Eng. J.* 454 (2023), 139993, <https://doi.org/10.1016/j.cej.2022.139993>.
- [14] H. Zhu, W. Yang, Y. Reo, G. Zheng, S. Bai, A. Liu, Y.-Y. Noh, Tin perovskite transistors and complementary circuits based on A-site cation engineering, *Nat. Electron.* 6 (2023) 650–657, <https://doi.org/10.1038/s41928-023-01019-6>.
- [15] K. Wang, G. Xing, Q. Song, S. Xiao, Micro- and nanostructured lead halide perovskites: from materials to integrations and devices, *Adv. Mater.* 33 (2021) 2000306, <https://doi.org/10.1002/adma.202000306>.
- [16] M. Li, R. Sun, J. Chang, J. Dong, Q. Tian, H. Wang, Z. Li, P. Yang, H. Shi, C. Yang, Z. Wu, R. Li, Y. Yang, A. Wang, S. Zhang, F. Wang, W. Huang, T. Qin, Orientated crystallization of FA-based perovskite via hydrogen-bonded polymer network for efficient and stable solar cells, *Nat. Commun.* 14 (2023) 573, <https://doi.org/10.1038/s41467-023-36224-6>.
- [17] Y. Wang, L. Li, Z. Wu, R. Zhang, J. Hong, J. Zhang, H. Rao, Z. Pan, X. Zhong, Self-driven prenucleation-induced perovskite crystallization enables efficient perovskite solar cells, *Angew. Chemie Int. Ed.* 62 (2023), <https://doi.org/10.1002/anie.202302342>.
- [18] B. Wang, Q. Cheng, G. Huang, Y. Yue, W. Zhang, X. Li, Y. Li, W. Du, X. Liu, H. Zhang, Y. Zhang, H. Zhou, Sulfonium-cations-assisted intermediate engineering for quasi-2D perovskite solar cells, *Adv. Mater.* 35 (2023), <https://doi.org/10.1002/adma.202207345>.
- [19] X. Yue, X. Zhao, B. Fan, Y. Yang, L. Yan, S. Qu, H. Huang, Q. Zhang, H. Yan, P. Cui, J. Ji, J. Ma, M. Li, Surface regulation through dipolar molecule boosting the

- efficiency of mixed 2D/3D perovskite solar cell to 24%, *Adv. Funct. Mater.* 33 (2023) <https://doi.org/10.1002/adfm.202209921>.
- [20] D. Gao, R. Li, X. Chen, C. Chen, C. Wang, B. Zhang, M. Li, X. Shang, X. Yu, S. Gong, T. Pauporté, H. Yang, L. Ding, J. Tang, J. Chen, Managing interfacial defects and carriers by synergistic modulation of functional groups and spatial conformation for high-performance perovskite photovoltaics based on vacuum flash method, *Adv. Mater.* 35 (2023), <https://doi.org/10.1002/adma.202301028>.
- [21] F. Wang, X. Zhou, X. Liang, D. Duan, C.-Y. Ge, H. Lin, Q. Zhu, L. Li, H. Hu, Solvent engineering of ionic liquids for stable and efficient perovskite solar cells, *Adv. Energy Sustain. Res.* 4 (2023), <https://doi.org/10.1002/aesr.202200140>.
- [22] X. Liang, D. Duan, M.B. Al-Handawi, F. Wang, X. Zhou, C. Ge, H. Lin, Q. Zhu, L. Li, P. Naumov, H. Hu, The Role of ionic liquids in performance enhancement of two-step perovskite photovoltaics, *Sol. RRL* 7 (2023), <https://doi.org/10.1002/solr.202200856>.
- [23] S. Yang, Y. Duan, Z. Liu, S. (Frank) Liu, Recent advances in CsPbX<sub>3</sub> perovskite solar cells: focus on crystallization characteristics and controlling strategies, *Adv. Energy Mater.* 13 (2023), <https://doi.org/10.1002/aenm.202201733>.
- [24] M. Liu, L. Bi, W. Jiang, Z. Zeng, S. Tsang, F.R. Lin, A.-K.-Y. Jen, Compact hole-selective self-assembled monolayers enabled by disassembling micelles in solution for efficient perovskite solar cells, *Adv. Mater.* (2023), <https://doi.org/10.1002/adma.202304415>.
- [25] M. Singh, M. Abdelsamie, Q. Li, T. Kodalle, D.-K. Lee, S. Arnold, D.R. Ceratti, J. L. Slack, C.P. Schwartz, C.J. Brabec, S. Tao, C.M. Sutter-Fella, Effect of the precursor chemistry on the crystallization of triple cation mixed halide perovskites, *Chem. Mater.* 35 (2023) 7450–7459, <https://doi.org/10.1021/acs.chemmater.3c00799>.
- [26] C. Xu, Z. Zhang, S. Zhang, H. Si, S. Ma, W. Fan, Z. Xiong, Q. Liao, A. Sattar, Z. Kang, Y. Zhang, Manipulation of perovskite crystallization kinetics via lewis base additives, *Adv. Funct. Mater.* 31 (2021) 2009425, <https://doi.org/10.1002/adfm.202009425>.
- [27] Y. Chen, J. Hu, Z. Xu, Z. Jiang, S. Chen, B. Xu, X. Xiao, X. Liu, K. Forberich, C. J. Brabec, Y. Mai, F. Guo, Managing phase orientation and crystallinity of printed dion-jacobson 2D perovskite layers via controlling crystallization kinetics, *Adv. Funct. Mater.* 32 (2022) 2112146, <https://doi.org/10.1002/adfm.202112146>.
- [28] M. Qin, H. Xue, H. Zhang, H. Hu, K. Liu, Y. Li, Z. Qin, J. Ma, H. Zhu, K. Yan, G. Fang, G. Li, U. Jeng, G. Brocks, S. Tao, X. Lu, Precise control of perovskite crystallization kinetics via sequential a-site doping, *Adv. Mater.* 32 (2020) 2004630, <https://doi.org/10.1002/adma.202004630>.
- [29] C. Yin, M. Liu, Z. Zhang, M. Wei, X. Shi, Y. Zhang, J. Wang, Y. Wang, Perpendicular alignment of covalent organic framework (COF) pore channels by solvent vapor annealing, *J. Am. Chem. Soc.* 145 (2023) 11431–11439, <https://doi.org/10.1021/jacs.3c03198>.
- [30] M. Wang, Y. Wang, J. Zhao, J. Zou, X. Liang, Z. Zhu, J. Zhu, H. Wang, Y. Wang, F. Pan, Z. Jiang, Electrochemical interfacial polymerization toward ultrathin COF membranes for brine desalination, *Angew. Chemie Int. Ed.* 62 (2023), <https://doi.org/10.1002/anie.202219084>.
- [31] J. He, H. Liu, F. Zhang, X. Li, S. Wang, In situ synthesized 2D covalent organic framework nanosheets induce growth of high-quality perovskite film for efficient and stable solar cells, *Adv. Funct. Mater.* 32 (2022) 2110030, <https://doi.org/10.1002/adfm.202110030>.
- [32] J. Zhang, J. Duan, Q. Guo, Q. Zhang, Y. Zhao, H. Huang, Y. Duan, Q. Tang, A universal grain “cage” to suppress halide segregation of mixed-halide inorganic perovskite solar cells, *ACS Energy Lett.* 7 (2022) 3467–3475, <https://doi.org/10.1021/acsenergylett.2c01771>.
- [33] R. Nie, X. Chen, Z. Li, W. Chu, S. Ma, C. Li, X. Liu, Y. Chen, Z. Zhang, W. Guo, Efficient and stable perovskite solar cells by build-in  $\pi$ -columns and ionic interfaces in covalent organic frameworks, *Nano Res.* 16 (2023) 9387–9397, <https://doi.org/10.1007/s12274-023-5603-4>.
- [34] J. He, H. Liu, F. Zhang, X. Li, S. Wang, In situ synthesized 2D covalent organic framework nanosheets induce growth of high-quality perovskite film for efficient and stable solar cells, *Adv. Funct. Mater.* 32 (2022), <https://doi.org/10.1002/adfm.202110030>.
- [35] R. Nie, W. Chu, Z. Li, H. Li, S. Chen, Y. Chen, Z. Zhang, X. Liu, W. Guo, S. Il Seok, Simultaneously suppressing charge recombination and decomposition of perovskite solar cells by conjugated covalent organic frameworks, *Adv. Energy Mater.* 12 (2022) 2200480, <https://doi.org/10.1002/aenm.202200480>.
- [36] J. Guo, G. Meng, X. Zhang, H. Huang, J. Shi, B. Wang, X. Hu, J. Yuan, W. Ma, Dual-interface modulation with covalent organic framework enables efficient and durable perovskite solar cells, *Adv. Mater.* (2023), <https://doi.org/10.1002/adma.202302839>.
- [37] C.-Q. Han, X. Sun, X. Liang, L. Wang, H. Hu, X.-Y. Liu, Benzothiadiazole and its derivative-based sp<sup>2</sup> carbon-conjugated covalent organic frameworks for photocatalytic hydrogen generation, *J. Mater. Chem. C* (2023), <https://doi.org/10.1039/D3TC02305B>.
- [38] E. Jin, K. Geng, S. Fu, M.A. Addicoat, W. Zheng, S. Xie, J. Hu, X. Hou, X. Wu, Q. Jiang, Q. Xu, H.I. Wang, D. Jiang, Module-patterned polymerization towards crystalline 2D sp<sup>2</sup>-Carbon covalent organic framework semiconductors, *Angew. Chemie Int. Ed.* 61 (2022), <https://doi.org/10.1002/anie.202115020>.
- [39] X. Liang, K. Zhou, D. Duan, F. Wang, C. Ge, X. Zhou, M. Yuan, Y. Shi, H. Lin, Q. Zhu, G. Li, H. Hu, Metal-organic framework nanocrystals enabled efficient and durable two-step perovskite photovoltaics, *Chem. Eng. J.* 459 (2023), 141524, <https://doi.org/10.1016/j.cej.2023.141524>.
- [40] J. Wu, M.-H. Li, J.-T. Fan, Z. Li, X.-H. Fan, D.-J. Xue, J.-S. Hu, Regioselective multisite atomic-chlorine passivation enables efficient and stable perovskite solar cells, *J. Am. Chem. Soc.* 145 (2023) 5872–5879, <https://doi.org/10.1021/jacs.2c13307>.
- [41] J. Sun, B. Li, L. Hu, J. Guo, X. Ling, X. Zhang, C. Zhang, X. Wu, H. Huang, C. Han, X. Liu, Y. Li, S. Huang, T. Wu, J. Yuan, W. Ma, Hybrid block copolymer/perovskite heterointerfaces for efficient solar cells, *Adv. Mater.* 35 (2023), <https://doi.org/10.1002/adma.202206047>.
- [42] Z. Yi, B. Xiao, X. Li, Y. Luo, Q. Jiang, J. Yang, Novel dual-modification strategy using Ce-containing compounds toward high-performance flexible perovskite solar cells, 1 Z. Yi, B. Xiao, X. Li, Y. Luo, Q. Jiang J. Yang, *Nano Energy*, 2023, 109, 108241. *Nano Energy*. 109 (2023) 108241. <https://doi.org/10.1016/j.nanoen.2023.108241>.
- [43] R. Nie, W. Chu, Z. Li, H. Li, S. Chen, Y. Chen, Z. Zhang, X. Liu, W. Guo, S. Il Seok, Simultaneously suppressing charge recombination and decomposition of perovskite solar cells by conjugated covalent organic frameworks, *Adv. Energy Mater.* 12 (2022), <https://doi.org/10.1002/aenm.202200480>.
- [44] J. Dou, C. Zhu, H. Wang, Y. Han, S. Ma, X. Niu, N. Li, C. Shi, Z. Qiu, H. Zhou, Y. Bai, Q. Chen, Synergistic effects of Eu-MOF on perovskite solar cells with improved stability, *Adv. Mater.* 33 (2021), <https://doi.org/10.1002/adma.202102947>.
- [45] Q. Liang, K. Liu, M. Sun, Z. Ren, P.W.K. Fong, J. Huang, M. Qin, Z. Wu, D. Shen, C. Lee, J. Hao, X. Lu, B. Huang, G. Li, Manipulating crystallization kinetics in high-performance blade-coated perovskite solar cells via cosolvent-assisted phase transition, *Adv. Mater.* 34 (2022) 2200276, <https://doi.org/10.1002/adma.202200276>.
- [46] H. Xiao, C. Zuo, K. Yan, Z. Jin, Y. Cheng, H. Tian, Z. Xiao, F. Liu, Y. Ding, L. Ding, Highly efficient and air-stable inorganic perovskite solar cells enabled by poly(lactic acid) modification, *Adv. Energy Mater.* (2023), <https://doi.org/10.1002/aenm.202300738>.
- [47] W. Sheng, J. He, J. Yang, Q. Cai, S. Xiao, Y. Zhong, L. Tan, Y. Chen, Multifunctional metal-organic frameworks capsules modulate reactivity of lead iodide toward efficient perovskite solar cells with UV resistance, *Adv. Mater.* 35 (2023), <https://doi.org/10.1002/adma.202301852>.